

# Linearisation with Cosmological Perturbation Theory

Francisco-Shu Kitaura<sup>1,2\*</sup> and Raul E. Angulo<sup>2†</sup>

<sup>1</sup> *Leibniz-Institut für Astrophysik Potsdam (AIP), An der Sternwarte 16, D-14482 Potsdam, Germany*

<sup>2</sup> *Max-Planck Institut für Astrophysik (MPA), Karl-Schwarzschildstr. 1, D-85748 Garching, Germany*

30 November 2011

## ABSTRACT

We propose a new method to linearise cosmological mass density fields using higher order Lagrangian perturbation theory (LPT). We demonstrate that a given density field can be expressed as the sum of a linear and a nonlinear component which are tightly coupled to each other by the tidal field tensor within the LPT framework. The linear component corresponds to the initial density field in Eulerian coordinates, and its mean relation with the total field can be approximated by a logarithm (giving theoretical support to recent attempts to find such component). We also propose to use a combination of the linearisation method and the continuity equation to find the mapping between Eulerian and Lagrangian coordinates. In addition, we note that this method opens the possibility of use directly higher order LPT on nonlinear fields. We test our linearization scheme by applying it to the  $z \sim 0.5$  density field from an  $N$ -body simulation. We find that the linearised version of the full density field can be successfully recovered on  $\gtrsim 5 h^{-1}\text{Mpc}$ , reducing the skewness and kurtosis of the distribution by about one and two orders of magnitude, respectively. This component can also be successfully traced back in time, converging towards the initial unevolved density field at  $z \sim 100$ . We anticipate a number of applications of our results, from predicting velocity fields to estimates of the initial conditions of the universe, passing by improved constraints on cosmological parameters derived from galaxy clustering via reconstruction methods.

**Key words:** (cosmology:) large-scale structure of Universe – galaxies: clusters: general – catalogues – galaxies: statistics

## 1 INTRODUCTION

The present-day mass density field contains information about the fundamental pillars of modern cosmology. It is a mixture and cross-talk between the primordial hierarchy of correlation functions of fluctuations, the law of gravity and the value of cosmological parameters. Unfortunately, disentangling all these ingredients and extracting useful information about them is not a trivial task. On large scales this is still relatively simple; linear theory applies and different Fourier modes evolve independently from each other. In fact, thanks to these features, cosmological parameters are almost routinely constrained using large-scale galaxy clustering. (see e.g. Cole et al. 2005; Eisenstein et al. 2005; Hütsi 2006; Blake et al. 2007; Percival et al. 2010; Blake et al. 2011). The description of small scales is much more difficult; highly nonlinear processes are in place, gravity couples perturbations on different scales and additional complica-

tions arise from nonlinear galaxy biasing and redshift space distortions.

Different approaches have been proposed to recover the primordial, linear and Gaussian, density field on medium- or small-scales – a process usually referred to as “Gaussianisation” or “Linearisation”. The majority are based on a local rank-ordered mapping, where the  $n$ -th largest density fluctuation in one field causes the  $n$ -th largest perturbation in the other. Examples of this are; the logarithm of the local density field (Neyrinck et al. 2009, 2011; Joachimi et al. 2011), a local Gaussianisation assuming that the primordial probability distribution function (PDF) of densities is known (Weinberg 1992; Yu et al. 2011), and applying linear or closely linear filters (by simple Gaussianisation (Neyrinck et al. 2011) or more sophisticated Wiener-filtering with a wavelet truncation (Zhang et al. 2011)). Although these methods have shown to accomplish their goals (with different degrees of success), they still lack a rigorous theoretical motivation and support. Additionally, gravity is a nonlocal process, where the evolution of a density fluctuation is not only determined by its amplitude, but it also depends on the surrounding tidal field (Rimes & Hamilton 2006, 2005).

\* E-mail: kitaura@aip.de, Karl-Schwarzschild fellow

† E-mail: rangulo@mpa-garching.mpg.de

Therefore, a rank-preserving mapping can not be correct in detail.

In this work we propose and explore another way to recover the initial density field. Our method takes advantage of the fact that an initial, linear, field and its gravitationally evolved counterpart are not independent from each other, but are related through the tidal field tensor. This gives us an extra piece of information to constrain and improve their mapping. Furthermore, the tidal tensor can be predicted analytically, and be fully specified by a linear field, using higher order Lagrangian perturbation theory (LPT, Buchert et al. 1994; Bouchet et al. 1995; Scoccimarro 1998; Bernardeau et al. 2002). Putting these ingredients together allows us to uniquely identify the initial density field which, evolved under 2LPT gravity, would give rise to the final density field we aim to linearise. We note that similar approaches have been explored in the past but with limited success and different scopes (see Gramann 1993; Monaco & Efstathiou 1999).

With this physically motivated Gaussianisation process we can interpret rank-ordering mappings, in particular, the widely used logarithmic transformation. Explicitly, we find that the mean transformation between the nonlinear and LPT linearised density fields can be approximated by a logarithmic function, consistent with the solution of the linear version of the continuity equation. In addition, we demonstrate that the linearised field is a good estimate of the initial field, not at its respective (earlier) time but at the present. Thus, one needs to trace this linearised field back in time, or, equivalently, to find the transformation from Eulerian to Lagrangian coordinates, if this field is to be used for constrained simulations and/or improved cosmological parameters constraints. One exception occurs on large scales or high redshifts, where Eulerian and Lagrangian coordinates coincide.

We validate these ideas by applying our 2LPT linearisation method to a density field extracted from a cosmological  $N$ -body simulation. The PDF of the resulting linearised field is closely described by a Gaussian function. In addition, this field correlates with the high redshift outputs of the simulation, much more than the original field. The correlation increases further when the linearised field is traced back in time. All this on scales even as small as  $\sim 5 h^{-1} \text{Mpc}$ .

An useful consequence of a Gaussianisation, is that the linearised field in Eulerian coordinates can be used as an input for Lagrangian perturbation theory and consistently predict the associated velocity, displacement and future density fields. A comparison between estimations of the displacement field in Eulerian coordinates and the linearised field, as given by the logarithmic transformation, was provided in a recent paper (Falck et al. 2011). The latter field could be specially useful for reconstruction of the large-scale density field in general, and of Baryonic Acoustic Oscillations (BAO) in particular (see Eisenstein et al. 2007; Noh et al. 2009; Mehta et al. 2011). In a companion paper we show that an accurate estimation of peculiar velocities can also be obtained in this way. In this case, the usage of our estimation of the linear field yields to results superior to those obtained by using a logarithmic transformation (Kitaura et al. 2011). In subsequent papers we will address other applications of the linearised density field.

The paper is structured as follows. In section §2 we present the theoretical basis for our 2LPT and for the loga-

rithmic linearisation. We also derive the equations governing the time-reversal of the linearised field. We discuss a practical implementation in §3 and discuss its performance once applied to a  $N$ -body simulation in §3. Finally, we present our conclusions.

## 2 THEORY

In this section we recap Lagrangian perturbation theory and show how a gravitationally evolved density field can be expanded into a linear and a nonlinear component. We also show that the widely used lognormal transformation gives an estimate of this linear component in Eulerian coordinates. Finally, we derive the equations to trace a density field back in time, allowing us to express the linear component (or linearised field) in Lagrangian coordinates, which then corresponds to the actual initial density field.

### 2.1 Lagrangian perturbation theory linearisation

Let us start by considering the mapping between the comoving coordinates of a set of test particles at two redshifts  $\mathbf{x}(z)$  and  $\mathbf{q}(z_0)$ , with  $z < z_0$ . In Lagrangian perturbation theory this relation is expressed via a displacement field,  $\Psi(\mathbf{q})$  (see e. g. Bernardeau et al. 2002):

$$\mathbf{x} = \mathbf{q} + \Psi(\mathbf{q}). \quad (1)$$

which defines a unique mapping between  $\mathbf{q}$  and  $\mathbf{x}$  (usually referred to as Lagrangian and Eulerian coordinates). We note that such a description of gravitational clustering starts breaking down when shell-crossing begins. If we further assume that the test particles were initially homogeneously distributed, then we can write the following mass conservation relation:

$$\rho(\mathbf{x}, z) d\mathbf{x} = \langle \rho(z_0) \rangle d\mathbf{q}. \quad (2)$$

The inverse of the Jacobian of the coordinate transformation defines the overdensity field,  $\delta \equiv \rho/\langle \rho \rangle - 1$ ,

$$1 + \delta(\mathbf{x}(\mathbf{q}, z)) = \mathbf{J}(\mathbf{q}, z)^{-1}, \quad (3)$$

with

$$\mathbf{J}(\mathbf{q}, z) \equiv \left| \frac{\partial \mathbf{x}}{\partial \mathbf{q}} \right|. \quad (4)$$

Combining Eqs. (1) and (3) we obtain an expression for the density in Lagrangian coordinates  $\mathbf{q}$  using an identity for determinants of matrices and assuming curl-free velocity fields ( $\Psi = -\nabla\Theta$ , for a discussion on this see Kitaura et al. 2011):

$$\begin{aligned} \delta(\mathbf{q}, z) &= |1 + \nabla_{\mathbf{q}} \cdot \Psi(\mathbf{q}, z)|^{-1} - 1 \\ &= -\nabla_{\mathbf{q}} \cdot \Psi(\mathbf{q}, z) + \mu^{(2)}[\Theta](\mathbf{q}, z) + \mu^{(3)}[\Theta](\mathbf{q}, z), \end{aligned} \quad (5)$$

where the subscripts  $\mathbf{q}$  refer to partial derivatives with respect to  $\mathbf{q}$ . The second term in Jacobian expansion is given by;

$$\mu^{(2)}[\Theta](\mathbf{q}, z) = \sum_{i>j} \left( \Theta_{,ii}(\mathbf{q}, z)\Theta_{,jj}(\mathbf{q}, z) - [\Theta_{,ij}(\mathbf{q}, z)]^2 \right), \quad (6)$$

where we use the abbreviation  $\Theta_{,ij} \equiv \partial^2 \Theta / \partial q_i \partial q_j$ . The third term is:

$$\mu^{(3)}[\Theta] = \det(\Theta_{,ij}). \quad (7)$$

Note that the density field at redshift  $z$  expressed in Lagrangian coordinates,  $\delta(\mathbf{x}(\mathbf{q}, z))$ , is fully determined by the displacement field. This field in turn can be calculated within 2nd order LPT (2LPT), in particular it is given in terms of two potentials:

$$\Psi(\mathbf{q}, z) = -D(z)\nabla_q \phi^{(1)}(\mathbf{q}) + D_2(z)\nabla_q \phi^{(2)}(\mathbf{q}), \quad (8)$$

and consequently;

$$\Theta(\mathbf{q}, z) = D(z)\phi^{(1)}(\mathbf{q}) - D_2(z)\phi^{(2)}(\mathbf{q}), \quad (9)$$

where  $D$  is the linear growth factor, and  $D_2$  the second order growth factor given by  $D_2 = \alpha D^2$  and  $\alpha \approx -3/7$ . The linear  $\phi^{(1)}$  and nonlinear potential  $\phi^{(2)}$  are obtained by solving a pair of Poisson equations:  $\nabla_q^2 \phi^{(1)}(\mathbf{q}) = \delta^{(1)}(\mathbf{q})$ , where  $\delta^{(1)}(\mathbf{q})$  is the linear overdensity, and  $\nabla_q^2 \phi^{(2)}(\mathbf{q}) = \delta^{(2)}(\mathbf{q})$ .

The term  $\delta^{(2)}(\mathbf{q})$  includes the effects of tidal forces and represents the ‘second-order overdensity’ which is related to the linear overdensity field by the following quadratic expression:

$$\delta^{(2)}(\mathbf{q}) = \sum_{i>j} \left( \phi_{,ii}^{(1)}(\mathbf{q})\phi_{,jj}^{(1)}(\mathbf{q}) - [\phi_{,ij}^{(1)}(\mathbf{q})]^2 \right). \quad (10)$$

Inserting these relations in Eq. (5) we get the desired decomposition of the field

$$\delta(\mathbf{q}, z) = \delta^L(\mathbf{q}, z) + \delta^{\text{NL}}(\mathbf{q}, z), \quad (11)$$

where  $\delta^L(\mathbf{q}, z) = D(z)\delta^{(1)}(\mathbf{q})$  is the linear component of the density field and the rest being the nonlinear part  $\delta^{\text{NL}}(\mathbf{q}, z) = -D_2(z)\delta^{(2)}(\mathbf{q}) + \mu^{(2)}[\Theta](\mathbf{q}, z) + \mu^{(3)}[\Theta](\mathbf{q}, z)$ . From now on we will also use the following notation for short  $\delta_D = \delta/D(z)$ .

Note that Eq. 11 is only a function of the coordinates  $\mathbf{q}$  and the redshift  $z$ . The full nonlinear density field  $\delta(\mathbf{q}, z)$  is expressed in Lagrangian coordinates while it naturally should be expressed in Eulerian coordinates. For the same reason we could write the same equation as a function of the Eulerian coordinates  $\mathbf{x}$ . We then get that the full nonlinear density field is a function of the linear component in Eulerian coordinates. We will use this result in either formulation and leave therefore the coordinate dependence out.

Integrating Eq. (11) we get an analogous expression for the full potential:

$$D(z)\phi_g = D(z)\phi^{(1)} + \phi^{\text{NL}} \quad (12)$$

with  $\phi^{\text{NL}} = -D_2(z)\phi^{(2)}[\phi^{(1)}] + \phi^{(2)}[\Theta(\phi^{(1)})] + \phi^{(3)}[\Theta(\phi^{(1)})]$  and following operator notation  $\phi^{(2)}[\phi] \equiv \nabla^{-2}\mu^{(2)}[\phi]$  and  $\phi^{(3)}[\phi] \equiv \nabla^{-2}\mu^{(3)}[\phi]$  with  $\phi$  being some field.

This equation tells us how an evolved gravitational potential is fully determined by its associated linear potential.

Therefore, linearising a field then becomes an inversion problem, which in section §3 we discuss how to solve.

## 2.2 Lognormal linearisation

Here we investigate the lognormal transformation as a mean to get an estimate of the linear component of the density field. Let us follow Coles & Jones (1991) and start with the continuity equation describing the matter content in the Universe as a fluid:

$$\frac{\partial \rho}{\partial t} + \frac{1}{a} \nabla \cdot (\rho \cdot \mathbf{u}) = 0, \quad (13)$$

which can be expanded

$$\frac{\partial \rho}{\partial t} + \frac{1}{a} (\mathbf{u} \cdot \nabla) \rho + \frac{1}{a} \rho \nabla \cdot \mathbf{u} = 0. \quad (14)$$

We can write this equation in Lagrangian coordinates introducing the total derivative

$$\frac{d\rho}{dt} = \frac{\partial \rho}{\partial t} + \frac{1}{a} (\mathbf{u} \cdot \nabla) \rho. \quad (15)$$

If we also switch to conformal time  $ad\tau = dt$  then we find

$$\frac{1}{\rho} \frac{d\rho}{d\tau} = -\nabla \cdot \mathbf{u} \quad (16)$$

As long as we can follow particles (no shell-crossings) we may also write the continuity equation as

$$\ln(1 + \delta) = - \int d\tau \nabla \cdot \mathbf{u}. \quad (17)$$

One must be especially careful at this point as the divergence of the peculiar velocity field in the right hand side of the latter equation is in Eulerian coordinates and not in Lagrangian coordinates (for such an approach see Matarrese et al. 1992). The expansion of this term is not straightforward for this reason. Note that the lognormal transformation will be equal to minus the divergence of the displacement field  $\delta^L = -\nabla \cdot \Psi$  *only* in linear Lagrangian perturbation theory.

According to LPT (see Eq. 3) we have yet another expression for the logarithm of the density field, which can be Taylor expanded using an identity for the Jacobian

$$\begin{aligned} \ln(1 + \delta) &= -\ln(J), \\ &= -\ln \left( 1 + \nabla_q \cdot \Psi + \mu^{(2)}[\Theta] - \mu^{(3)}[\Theta] \right), \\ &\simeq \delta^L + \delta^+, \end{aligned} \quad (18)$$

where the quantity  $\delta^+$  summarises all the higher order terms. Note that  $\delta^+$  will be a nonlocal and nonlinear function of  $\delta^L$ . Taking the ensemble average of the previous equation we find that

$$\langle \delta^+ \rangle = \mu = \langle \ln(1 + \delta) \rangle \quad (19)$$

and

$$\delta^L \simeq \ln(1 + \delta) - \mu \quad (20)$$

In this way we have demonstrated that first order Taylor expansion of the higher order corrections are given by the mean field:  $\langle \delta^+ \rangle = \mu$ . Note, that in reality the term  $\delta^+ = \delta^+(\mathbf{x}, z)$  will not be a homogeneous field. In order to improve this one has to make higher order expansions. The importance of computing the mean field  $\mu$  was especially emphasized in Kitaura et al. (2010). A way to compute this field from the linear field  $\delta^L$  was presented in Kitaura et al. (2010).

### 2.3 Time-reversal evolution equations: the Eulerian-Lagrangian approach

In this section we investigate different formulations of the continuity equation which permit to trace the structures back in time. In particular we find an expression which shows how the linear component can be iteratively traced back in time. For the derivation of such an equation we will combine the results from Lagrangian perturbation theory (based on the equation of motion) with an Eulerian formulation of the continuity equation.

Let us express the continuity equation as a function of the overdensity  $\delta$  and a scaled peculiar velocity given by  $\mathbf{v} \equiv \mathbf{u}/\dot{D} = \mathbf{u}/(fHD)$

$$\begin{aligned} \frac{\partial \delta}{\partial D} + \nabla \cdot ((1 + \delta) \mathbf{v}) &= 0, \\ \frac{\partial \delta}{\partial D} + (1 + \delta) \nabla \cdot \mathbf{v} + (\mathbf{v} \cdot \nabla) \delta &= 0. \end{aligned} \quad (21)$$

We could try to directly integrate this equation backw in time computing in each iteration the peculiar velocity field from the updated density field. However, let us derive a formulation of the continuity equation which can be better compared with previous works and ensures time-reversibility. Following Gramann (1993) we define the deviation from linear theory as

$$\delta_{gv} \equiv \delta/D - \delta_{\text{LPT}}/D = \delta/D + \nabla \cdot \mathbf{v} \text{ with } \delta_{\text{LPT}} \equiv -D \nabla \cdot \mathbf{v}.$$

We can then rewrite Eq. 21 as

$$\frac{\partial \delta}{\partial D} - \frac{\delta}{D} - D ((\nabla \cdot \mathbf{v})^2 + (\mathbf{v} \cdot \nabla) \nabla \cdot \mathbf{v}) + \delta_{gv} + D \nabla \cdot (\delta_{gv} \mathbf{v}) = 0. \quad (22)$$

Under the assumption that flows are irrotational:

$$(\nabla \cdot \mathbf{v})^2 + (\mathbf{v} \cdot \nabla) \nabla \cdot \mathbf{v} = \frac{1}{2} \nabla^2 v^2 + 2\delta^{(2)}[\phi_v] \text{ (with } \mathbf{v} = -\nabla \phi_v), \text{ Eq. 22 is simplified to}$$

$$\frac{\partial \delta}{\partial D} - \frac{\delta}{D} - D \left( \frac{1}{2} \nabla^2 v^2 + 2\mu^{(2)}[\phi_v] \right) + \delta_{gv} + D \nabla \cdot (\delta_{gv} \mathbf{v}) = 0. \quad (23)$$

Integrating the latter equation we obtain

$$\frac{\partial \phi_g}{\partial D} - \frac{1}{2} v^2 - 2\phi^{(2)}[\phi_v] + \frac{1}{D} \phi_{gv} + \nabla^{-2} \nabla \cdot (\delta_{gv} \mathbf{v}) = 0, \quad (24)$$

$$\text{with } \delta_{gv} = \nabla^2 \phi_{gv}.$$

#### 2.3.1 2nd order continuity equation

Let us consider only terms up to second order, i. e. neglecting terms involving  $\mathcal{O}(D^3)$ . The velocity is given by

$\mathbf{v}^{[2]} \equiv -\nabla \phi^{(1)} + \frac{f_2 D_2}{f D} \nabla \phi^{(2)}[\phi^{(1)}]$ . Hereafter the numbers in brackets denote the order of the expansion. Accordingly, the gravitational potential is given by  $\phi_g^{[2]} \equiv \phi^{(1)} + \frac{1}{D} (D^2 - D_2) \phi^{(2)}[\phi^{(1)}]$ . Note, that the peculiar velocity  $\mathbf{u}$  needs to be linear:  $\mathbf{v}^{[1]} \equiv -\nabla \phi^{(1)}$  in the quadratic term in the continuity equation. However, it will have a second order contribution in the deviation term

$$\delta_{gv}^{[2]} \equiv \left( \left( \frac{f_2}{f} - 1 \right) \frac{D_2}{D} + D \right) \delta^{(2)}[\phi^{(1)}]. \quad (25)$$

Putting all together we get

$$\frac{\partial \phi_g^{[2]}}{\partial D} - \frac{1}{2} (v^{[1]})^2 - \left( 1 + \left( \frac{f_2}{f} - 1 \right) \frac{D_2}{D} \right) \phi^{(2)}[\phi^{(1)}] = 0. \quad (26)$$

If we neglect the contribution of 2LPT ( $D_2 = 0$ ) we get the formula derived by Gramann (1993). Neglecting tidal forces ( $\phi^{(2)}[\phi^{(1)}] = 0$ ) we get the formula by Nusser & Dekel (1992).

#### 2.3.2 Higher order continuity equation

To go beyond the Zeldovich approximation in the velocity term say to 2nd order in Lagrangian perturbation theory one needs to consider at least 4th order terms in the continuity equation. The gravitational potential can be written according to §2.1 as  $\phi_g^{[\tilde{6}]} \equiv \phi^{(1)} - \frac{D_2}{D} \phi^{(2)}[\phi^{(1)}] + \frac{1}{D} (\phi^{(2)}[\Theta] + \phi^{(3)}[\Theta])$  with the symbol  $[\tilde{6}]$  indicating that the 6th order is incomplete. Note that the term  $\phi^{(3)}[\phi] \equiv \nabla^{-2} \mu^{(3)}[\phi]$  includes sixth order terms involving  $D^6$ . However a proper sixth order formulation would require including third order Lagrangian perturbation theory. To obtain the 4th order equation one would need to truncate that term. The deviation term is correspondingly given by

$$\phi_{gv}^{[\tilde{6}]} \equiv \left( \frac{f_2}{f} - 1 \right) \frac{D_2}{D} \phi^{(2)}[\phi^{(1)}] + \frac{1}{D} (\phi^{(2)}[\Theta] + \phi^{(3)}[\Theta]). \quad (27)$$

Finally, the continuity equation yields

$$\frac{\partial \phi_g^{[\tilde{6}]}}{\partial D} - \frac{1}{2} (v^{[2]})^2 - 2\phi^{(2)}[\phi_v^{[2]}] + \frac{1}{D} \phi_{gv}^{[\tilde{6}]} + \nabla^{-2} \nabla \cdot (\delta_{gv}^{[\tilde{6}]} \mathbf{v}^{[2]}) = 0. \quad (28)$$

## 3 NUMERICAL SOLUTION SCHEMES

Here we present our numerical approach to iteratively solve Eqs. 11 and 28. Note that the first equation determines the linear component of the field:  $\phi_g(\mathbf{x}, z) \rightarrow \phi^{(1)}(\mathbf{x}, z)$  (the arrow indicates that  $\phi^{(1)}$  is calculated from  $\phi_g$ ) and the second equation traces that component back in time yielding an estimate of the full component to an earlier cosmic time:  $\phi^{(1)}(\mathbf{x}, z) \rightarrow \phi_g(\mathbf{x}, z + \Delta z)$  (where  $\Delta z < 0$  in our case of study and in this case the arrow indicates that  $\phi_g$  at an earlier time is computed from  $\phi^{(1)}$ ).

(i)  $\phi_g(\mathbf{x}, z) \rightarrow \phi^{(1)}(\mathbf{x}, z)$

We propose to solve Eq. (12) iteratively by updating the

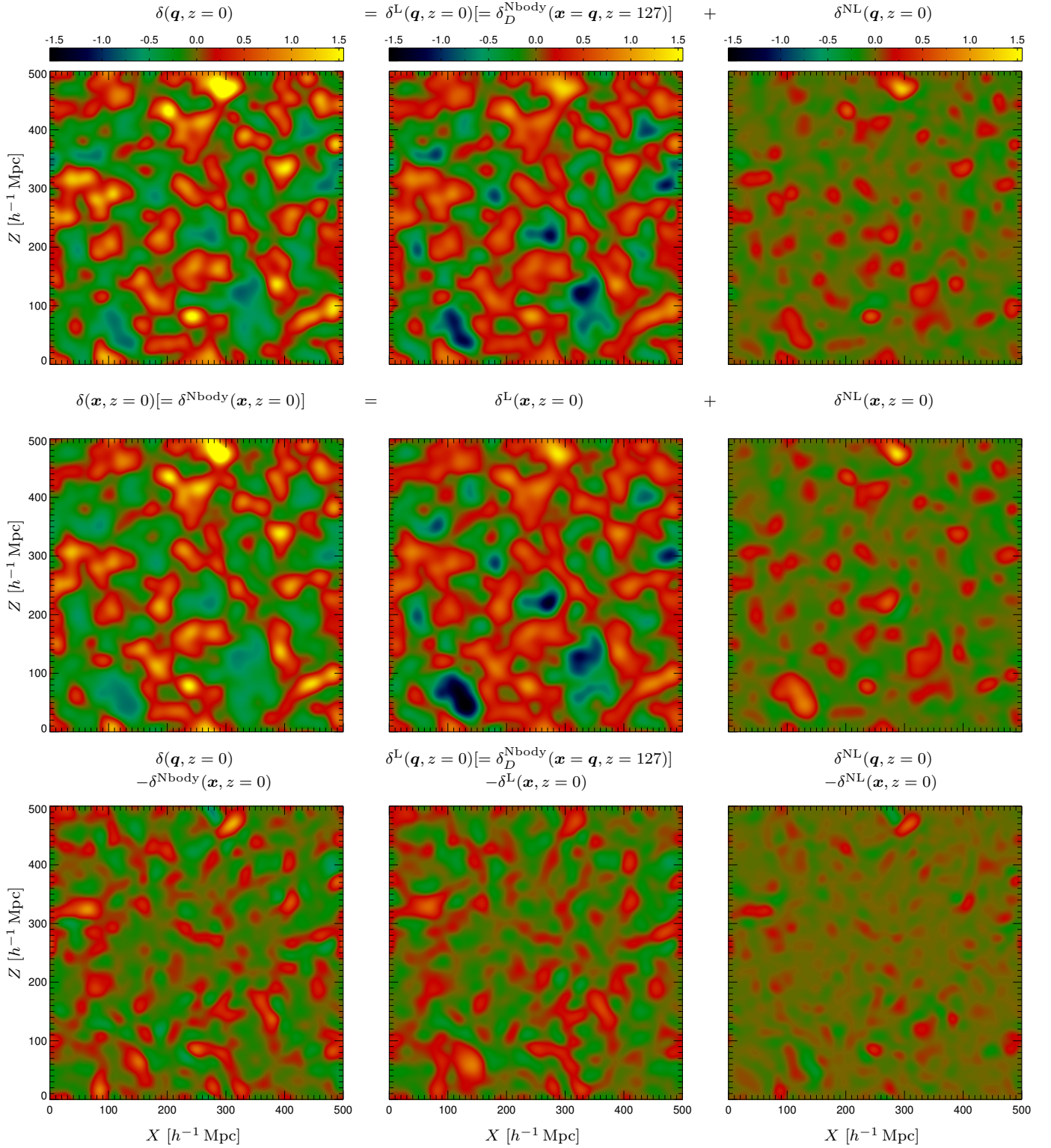


**Figure 1.** Slice through the density field of the Millennium Run after Gaussian smoothing with  $r_S^0 = 10 h^{-1} \text{ Mpc}$ . Upper left panel: forward solution of Eq. 6 taking as the linear field the Millennium Run at  $z = 127$ . Upper middle panel: Millennium Run at  $z = 127$ . Upper right panel: nonlinear component corresponding to the field in the middle panels. Central left panel: Millennium Run at  $z = 0$ . Central middle panel: iterative solution of the linear component. Central right panel: nonlinear component. Lower panels: differences between the corresponding fields in the upper panels and in the central panels.

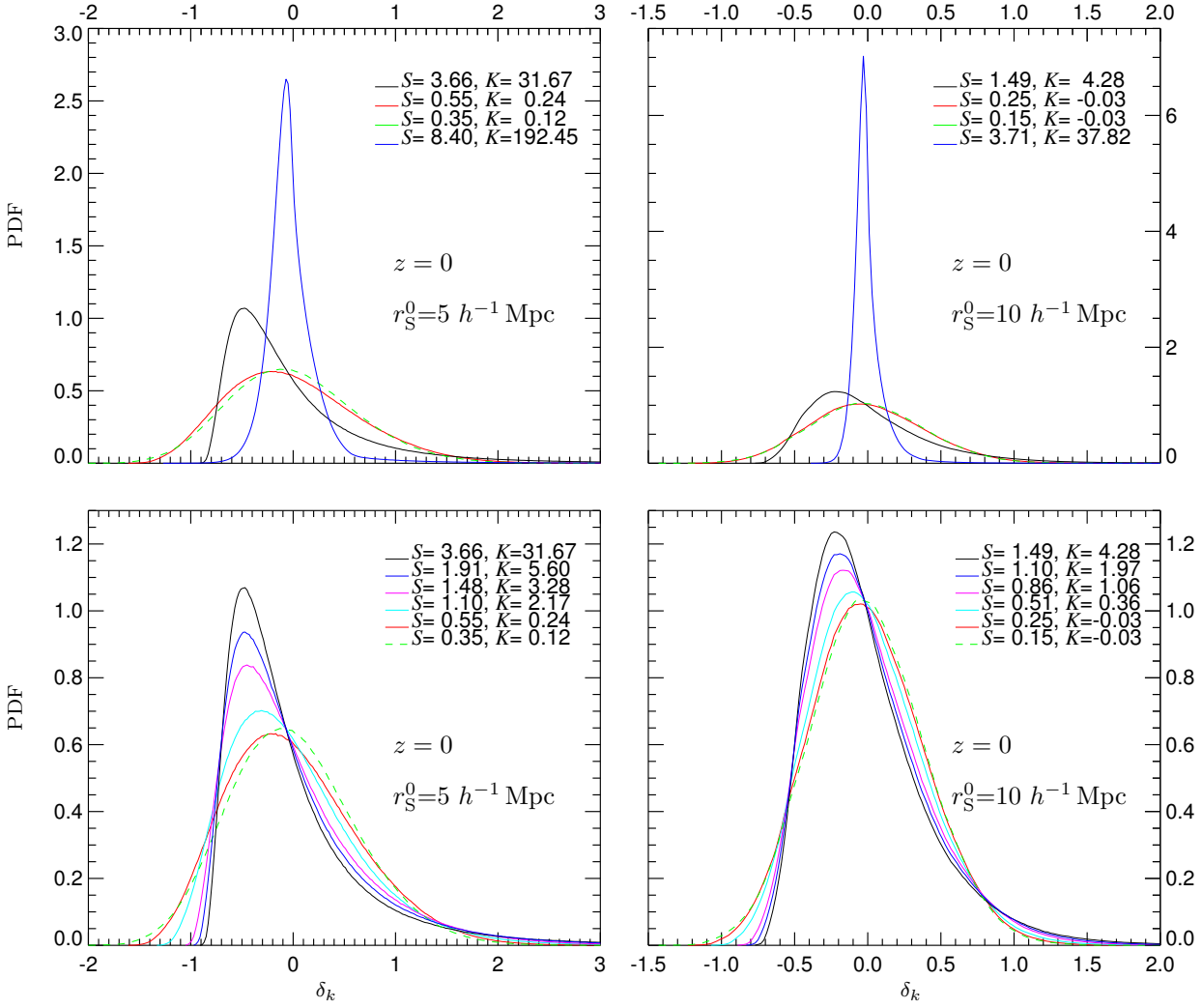


**Figure 2.** Matter probability distribution function (PDF) and corresponding skewness and kurtosis for  $\delta_k : \delta^{\text{Nbody}}(\mathbf{x}, z=0), \ln(1 + \delta^{\text{Nbody}}(\mathbf{x}, z=0)) - \mu, \delta^{\text{L}}(\mathbf{x}, z=0)$  and  $\delta^{\text{NL}}(\mathbf{x}, z=0)$ . Upper panels show the decomposition into a linear and a nonlinear component with an initial smoothing of  $r_S^0 = 5 h^{-1}$  Mpc (left) and  $10 h^{-1}$  Mpc (right), black: total field, red: linear component, blue: nonlinear component, green dashed: lognormal transformation. Lower panels show subsequent steps demonstrating the convergence of the linearisation process. Corresponding skewness  $S$  and kurtosis  $K$  are also indicated.

nonlinear component which depends on the linear potential  $\phi^{(1)}$ :

$$\phi_{i+1}^{(1)} = \phi_g + \tau_i \left( \frac{D_2}{D} \phi^{(2)} \left[ \phi_i^{(1)}, r_S^i \right] - \frac{1}{D} \left( \phi^{(2)} + \phi^{(3)} \right) \left[ \Theta(\phi_i^{(1)}), r_S^i \right] \right), \quad (29)$$

with  $r_S^i$  being a scale at iteration  $i$  which stabilises the solution. Here we use a Gaussian filter with decreasing smoothing radii.

(ii)  $\phi^{(1)}(\mathbf{x}, z) \rightarrow \phi_g(\mathbf{x}, z + \Delta z)$  To compute the time-reversal solution we follow Nusser & Dekel (1992); Gramann

(1993) and integrate the equation with finite time differences

$$\begin{aligned} \phi_g^{j+1}(\phi_{j+1}^{(1)}) &= \phi_j^{(1)} \\ &- \frac{D_{2j}}{D_j} \phi^{(2)}[\phi_j^{(1)}] + \frac{1}{D_j} \left( \phi^{(2)}[\Theta(\phi_j^{(1)})] + \phi^{(3)}[\Theta(\phi_j^{(1)})] \right) \\ &+ \Delta D_j \left( \frac{1}{2} \left( v(\phi_j^{(1)}) \right)^2 + 2\phi^{(2)}[\phi_v(\phi_j^{(1)})] - \frac{1}{D_j} \phi_{gv}(\phi_j^{(1)}) \right. \\ &\left. - \nabla^{-2} \nabla \cdot \left( \delta_{gv}(\phi_j^{(1)}) v(\phi_j^{(1)}) \right) \right). \end{aligned} \quad (30)$$

We should mention here that more adequate integration solvers should be studied which are mass conserving (solvers for hyperbolic partial differential equations). However, for the studies we are performing in this work the simple scheme presented above is adequate. One can notice that the form of the continuity equation as given by Eq. 30 is time-reversal as it remains invariant under the transformation:  $\phi^{(1)} \rightarrow -\phi^{(1)}$  and  $D \rightarrow -D$ .

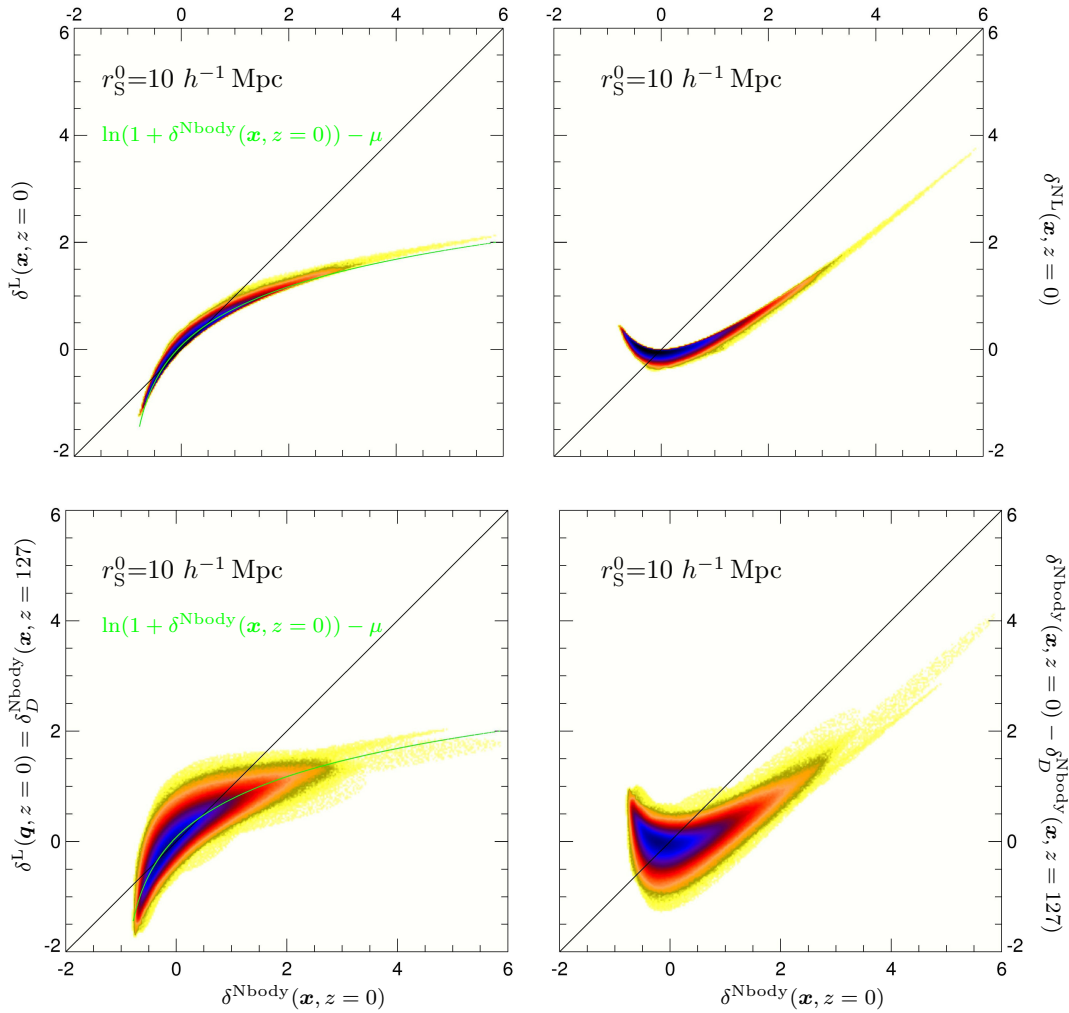


**Figure 3.** Cell-to-cell comparison after Gaussian smoothing with  $r_S^0 = 10 h^{-1} \text{Mpc}$  between the matter field  $\delta^{\text{Nbody}}(\mathbf{x}, z = 0)$  of the simulation at  $z = 0$  and Upper panels: Left: the iterative solution of the linear component at  $z = 0$  in Eulerian coordinates Right: the nonlinear component in Eulerian coordinates, Lower panels: Left: the simulation at  $z = 127$  representing the linear component in Lagrangian coordinates, Right: the difference between the simulation at  $z = 0$  and the field at  $z = 127$ . The green curve represents the lognormal transformation. Dark colour code indicates a larger number of cells and light colour code a lower number.

## 4 RESULTS

We carry out our numerical experiments using the Millennium Run. This simulation tracks the nonlinear evolution of more than 10 billion particles, in a box of comoving side-length  $500 h^{-1} \text{Mpc}$  (Springel et al. 2005). In particular, we consider the simulation at different redshifts ( $z = 0, 0.5, 1, 2, 3, 127$ ) gridded with nearest-grid-point (NGP) on a  $256^3$  mesh. To iteratively solve the combined Eulerian-Lagrangian set of equations described above, we have developed a parallel code that uses Fast Fourier Transforms to evaluate Laplacian operators and a finite differences method for divergence operators. We have dubbed this code as KIN-GEN<sup>1</sup>.

<sup>1</sup> KInetic GENeration of initial conditions (in Japanese: *origin*).

### 4.1 Linearisation

First, we show how Eq. 11 can be used to decompose the full nonlinear density field into a linear component and a nonlinear one. Since LPT breaks down when shell-crossing becomes dominant, we have to smooth the density field to suppress the power on small scales. We apply here a Gaussian-kernel with different smoothing radii 5 and  $10 h^{-1} \text{Mpc}$ . We also note that the operation of convolution does not commute with the linearisation. Therefore, we need to ensure that this does not seriously affect our results by comparing with the true linear field, i. e. with the initial conditions of the simulation as we show below. In the upper panels of Fig. 1 we solve Eq. 11 forwards given a linear density field taking the first snapshot of the simulation at  $z = 127$  which we define as the linear component in Lagrangian coordinates:  $\delta^{\text{L}}(\mathbf{q}, z = 0) = \delta_{\text{D}}^{\text{Nbody}}(\mathbf{x} = \mathbf{q}, z = 127)$  (middle panel) and computing the nonlinear component shown in the right panel  $\delta^{\text{NL}}(\mathbf{q}, z = 0)$ . Adding both components we get an estimate of the full nonlinear density field at  $z = 0$ :

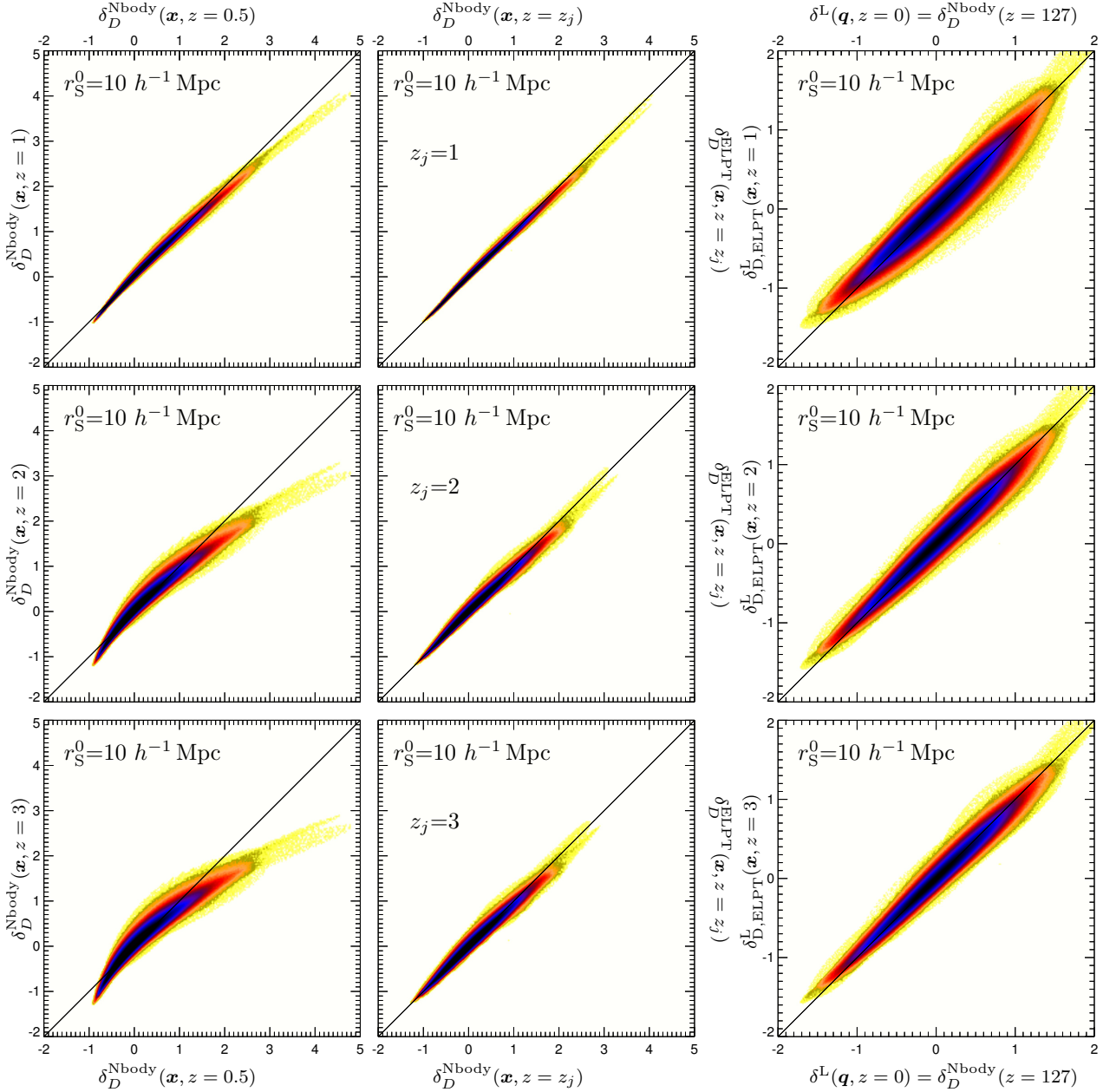


**Figure 4.** Left panels: cell-to-cell comparison after Gaussian smoothing with  $r_S^0 = 10 h^{-1} \text{Mpc}$  between the simulation at  $z = 0.5$ :  $\delta_D^{\text{Nbody}}(\mathbf{x}, z = 0.5)$  and the simulation at different redshifts  $\delta_D^{\text{Nbody}}(\mathbf{x}, z_j)$ . Middle panels: cell-to-cell comparison between the simulation at different redshifts  $\delta_D^{\text{Nbody}}(\mathbf{x}, z_j)$  and the time-reversal reconstruction of the full nonlinear field at the same redshift  $\delta_{D,\text{ELPT}}^{\text{L}}(\mathbf{x}, z = z_j)$ . Right panels: cell-to-cell comparison between the simulation at  $z = 127$   $\delta^{\text{L}}(\mathbf{q}, z = 0) = \delta_D^{\text{Nbody}}(z = 127)$  and the linear component of the reconstruction at different redshifts:  $\delta_{D,\text{ELPT}}^{\text{L}}(\mathbf{x}, z = z_j)$ . Note that  $z_j$  runs for the following redshifts  $z_j = 1, 2, 3$ .

$\delta(\mathbf{q}, z = 0)$ . We can see that the nonlinear component is positive both in the high and the low density regions in such a way that the peaks get more clustered as can be seen in the left panel. On the contrary, the voids become less deep. This effect is only apparent as the linear component has been multiplied by the relative growth factor as explained above. However, one should note that all the quantities are in the same (Lagrangian) coordinates. The panels in the second row of Fig. 1 show analogous plots but starting from the full gravitationally evolved overdensity field at  $z = 0$  on the left  $\delta(\mathbf{x}, z = 0)$ . Here the linear and nonlinear components

are computed by numerically solving Eq. 11, as described in §3. Both upper and middle sets of panels look very similar, however, a careful inspection shows that the structures are shifted. This is more clearly shown in the lower panels in which the differences between both corresponding panels are shown. The reason is that while the upper panels show the different components in Lagrangian coordinates the middle panels show them in Eulerian ones.

The upper panels in Fig. 2 show the decomposition of the fields into a linear and a nonlinear component in a more quantitative way for two smoothing scales; 5 and 10

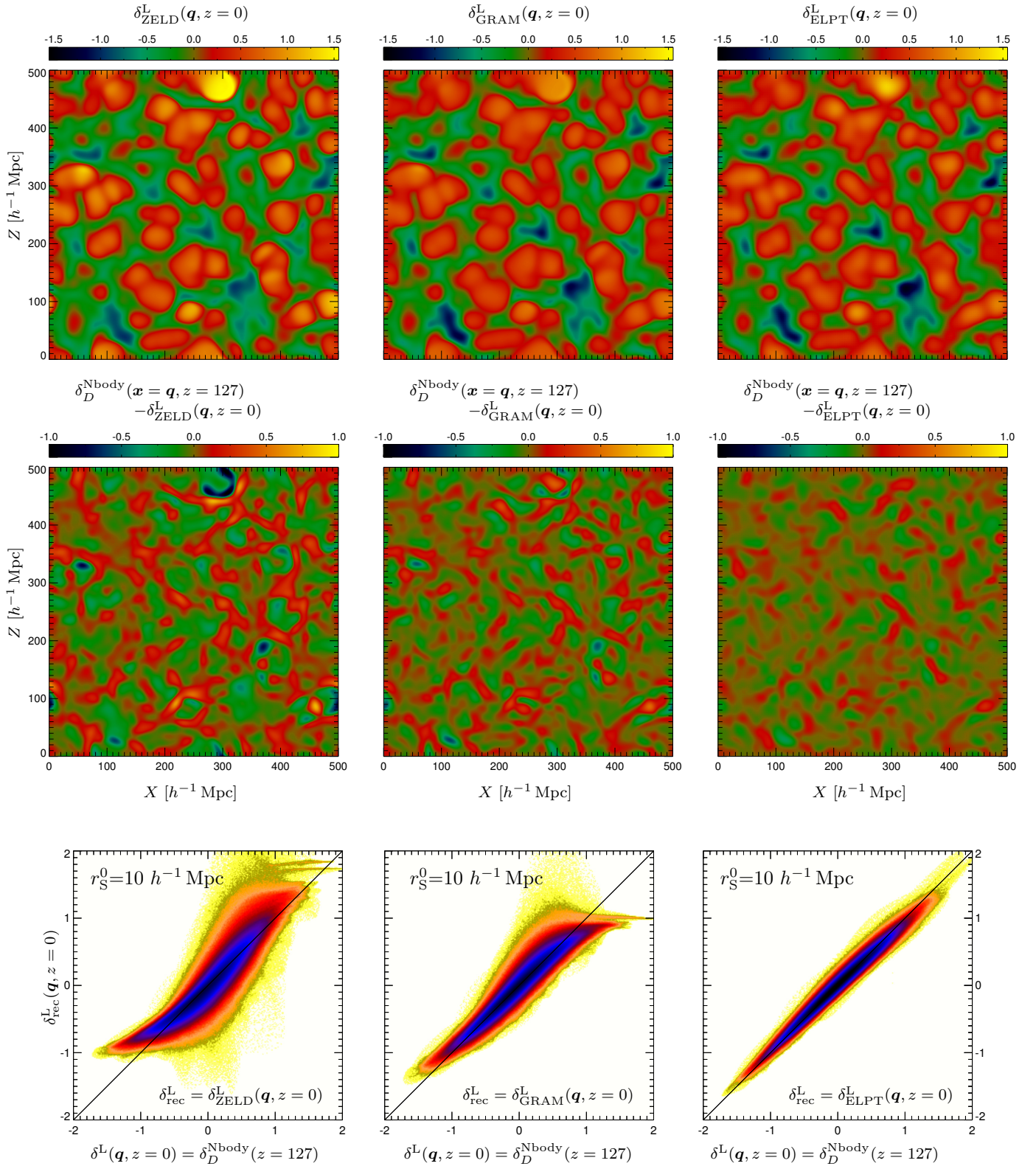


**Figure 5.** Upper panels: slices through the reconstructed initial conditions after Gaussian smoothing with  $r_S^0 = 10 h^{-1} \text{ Mpc}$  using Left: Zeldovich approximation, Middle: Gramann approximation, Right: this work. Middle panels: difference fields between the reconstruction and the actual initial field. Lower panels: cell-to-cell comparison between the reconstruction and the actual initial field.

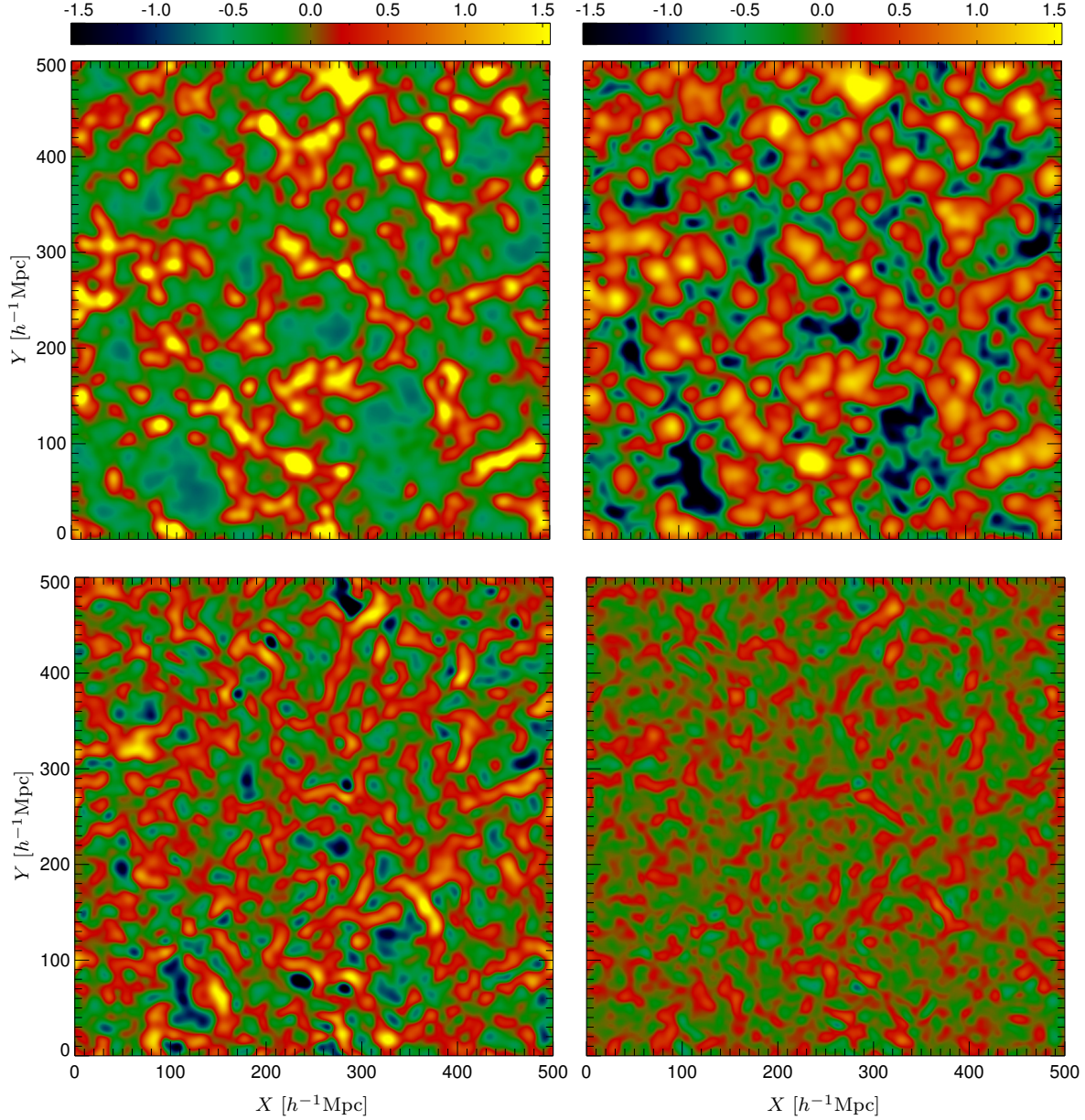


**Figure 6.** Upper left panel: slice through the simulation at  $z = 0.5$  with Gaussian smoothing of  $r_S^0 = 5 h^{-1} \text{Mpc}$ . Upper right panel: reconstructed initial condition. Lower panels: difference fields between the corresponding fields in the upper panels and the simulation at  $z = 127$ .

$h^{-1} \text{Mpc}$ . We show the PDF for the matter in the simulation at  $z = 0$  is shown (black line), the corresponding linear (red line) and nonlinear (blue line) components calculated with LPT (red line) and the lognormal linearisation (green line). We can see that the linearised fields are closely Gaussian distributed with low skewness ( $S$ ) and kurtosis ( $K$ ), whereas the full field, and even more dramatically the nonlinear component, have considerably large values for  $S$  and  $K$ . A careful inspection of the plots shows that the nonlinear component has not a symmetric PDF. This is better shown in Fig. 3. The lower panels show the convergent behaviour of

our numerical scheme, demonstrating its stable approach to the a solution with progressively smaller skewness and kurtosis.

To further see the effects of the LPT and lognormal linear mappings we compute the cell-to-cell correlation between the simulation at  $z = 0$ :  $\delta_D^{\text{Nbody}}(\mathbf{x}, z = 0)$  and the linear component  $\delta^{\text{L}}(\mathbf{x}, z = 0)$ . This can be seen in the upper left panel of Fig. 3. We find that the relation between both fields is highly nonlinear and that the lognormal mapping is in good agreement with the LPT linearisation. However, in the LPT case we see a scatter showing that the relation

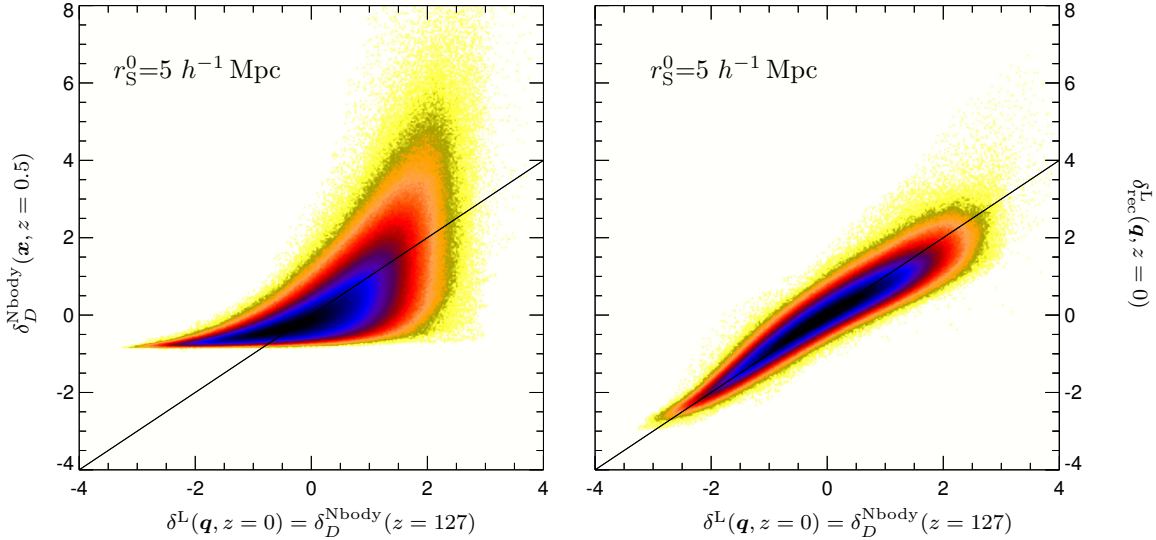


**Figure 7.** Cell-to-cell comparison between the simulation after Gaussian smoothing with  $r_s^0 = 5 h^{-1} \text{Mpc}$  at  $z = 127$  and Left: the simulation at  $z = 0.5$ , Right: the reconstruction of the initial field.

is nonlocal. We can see the non-Gaussian nature of the full nonlinear field in the x-axis, starting with an overdensity  $\delta \approx -1$  and reaching moderately large overdensities  $\delta > 6$ . The linearised field, shown in the y-axis, presents overdensities in the range  $-2 < \delta < 2$ . The comparison between the simulation at  $z = 0$ :  $\delta_D^{\text{Nbody}}(\mathbf{x}, z = 0)$  and the simulation at  $z = 127$ :  $\delta_D^{\text{Nbody}}(\mathbf{x} = \mathbf{q}, z = 127)$  shows a similar relation with a larger scatter. This is due to the fact that apart from the gravitational effects described in the upper panels of Fig. 1 there is a transformation from Lagrangian to Eulerian coordinates. It is remarkable how well the log-normal transformation traces the mean mapping between both fields. Additionally, the right panels in Fig. 3 show the corresponding nonlinear components. Here we can see how the nonlinear field gets positive both in the underdense and in the overdense regions compensating for the overestimation of the deepness of voids in linear theory and largely increasing the power in the high density regions.

## 4.2 Evolving the linear component back in time

The purpose of this section is to show that the linear component can be translated from Eulerian to Lagrangian coordinates. We will make such a demonstration solving Eq. 28 as presented in §3. In the numerical experiments of this section we take a starting redshift of  $z = 0.5$  which compensates for the high value of  $\sigma_8$  employed in the MS (Angulo & White 2010).

The results for different redshifts are shown in Fig. 4. The left panels show the cell-to-cell comparison between the simulation at  $z = 0.5$ :  $\delta_D^{\text{Nbody}}(\mathbf{x}, z = 0.5)$  and the simulation at different redshifts  $\delta_D^{\text{Nbody}}(\mathbf{x}, z_j)$  with  $z_j = 1, 2, 3$ . One can see in these plots how the relation between the fields gets increasingly more biased as expected. The central panels show the nearly unbiased cell-to-cell correlation between the simulation at different redshifts  $\delta_D^{\text{Nbody}}(\mathbf{x}, z_j)$  and the time-reversal reconstruction of the full nonlinear density field at the same redshift  $\delta_D^{\text{ELPT}}(\mathbf{x}, z = z_j)$ . This demon-

strates the success in recovering the full nonlinear field at scales of  $10 h^{-1} \text{Mpc}$ . The right panels show the linear component  $\delta_{\text{ELPT}}^{\text{L}}(\mathbf{x}, z_j)$  and the tight correlation with the actual initial conditions from the simulation. This correlation becomes larger with increasing smoothing scale. We have denoted the time-reversal reconstructed fields with the superscript ELPT standing for Eulerian-Lagrangian perturbation theory due to the combination of both approaches. We should note at this point that we have tried the less time-consuming approach of estimating the linear field at each time-step with the lognormal approximation. Sorrowfully, systematic errors propagate yielding significantly poorer solutions. We analyze this issue in more detail in Kitaura et al. (2011).

In Fig. 5 we show the performance of various grid based methods to recover the initial conditions including the Eulerian-Zeldovich approximation on the left (Nusser & Dekel 1992), Gramann (1993) in the middle and the one presented in this work on the right (see §2.3 for a derivation of the schemes). Here we integrate the ELPT equations back in time up to a redshift of  $z = 10$ . For higher redshifts we do not observe an appreciable shift in the structures, neither an improvement in the correlation to the initial field. Moreover, getting stable solutions of the linear component becomes more difficult, since the field we are trying to linearise is already quite linear. The bare eye inspection of the plots already shows that the structures are less smooth, the voids deeper, and the peaks better confined with increasing order of the continuity equation (see upper panels). As a consequence, the difference between the reconstructed fields and the initial conditions becomes smaller (see middle panels). From the comparison between the upper and the middle panels we can conclude that the largest differences are in the high density regions. The accuracy of the reconstruction is assessed in a more quantitative way in the cell-to-cell correlations (see lower panels). Clearly, the biases present in the Eulerian-Zeldovich approach are considerably reduced by taking higher order terms in the continuity equation.

The power of the Eulerian-Lagrangian reconstruction of the initial conditions is more clearly shown with smaller smoothing scales. Although our approach will break down at scales in which shell-crossing becomes important (as it is the case of LPT in general), we find that it is still extremely accurate even for scales  $\gtrsim 5 h^{-1} \text{Mpc}$  (this is further demonstrated in a companion paper Kitaura et al. 2011). In Fig. 6 we compare a slice through the simulation at  $z = 0.5$  with Gaussian smoothing of  $r_s^0 = 5 h^{-1} \text{Mpc}$  (upper left panel) with the Eulerian-Lagrangian reconstructed initial field (upper right panel). There, we can see how the clustered regions move away from each other and the voids become as strong as the peaks when going back in time – a signature of Gaussian fields. The lower panels hints on the correctness of our approach by showing the difference between the corresponding reconstructed fields and the simulation at  $z = 127$ . We can now appreciate how dipoles, caused by the incorrect position of large overdensities, are dramatically reduced with ELPT.

In Fig. 7 we show the cell-to-cell correlation for the simulation (after Gaussian smoothing with  $r_s^0 = 5 h^{-1} \text{Mpc}$ ) at  $z = 127$  and both the simulation at  $z = 0.5$  (left panel) and the reconstruction of the initial field with ELPT (right panel). This quantifies the accuracy of our time-reversal reconstruction. Here the improvement provided by the ELPT scheme in capturing the highly nonlinear and nonlocal relation between the initial and final fields is evident. The correlation between the reconstructed and the actual initial field gets significantly tighter and closely unbiased.

We define the true linear field  $\delta^{\text{LIN}}(\mathbf{k})$  as the one given by the first snapshot in the  $N$ -body simulation  $\delta_D^{\text{Nbody}}(\mathbf{k}, z_{\text{init}})$ :  $\delta^{\text{LIN}}(\mathbf{k}) \equiv \delta_D^{\text{Nbody}}(\mathbf{k}, z_{\text{init}})$  ( $z_{\text{init}} = 127$  in the case of the Millennium Run). Accordingly, the linear power-spectrum is given by:  $P^{\text{LIN}}(k) \equiv P_D^{\text{Nbody}}(k, z_{\text{init}})$ . We should note that the initial fields  $\hat{\delta}_D^{\text{rec}}(\mathbf{k}, z)$  we recover are on smooth fields. We need thus to deconvolve the fields to compare them to the unsmoothed linear field  $\delta^{\text{LIN}}(\mathbf{k})$ . For this reason we define a spherically averaged kernel  $\mathcal{K}(k, z) = \sqrt{\frac{P^{\text{LIN}}(k)}{P_D^{\text{rec}}(k, z)}}$  which permits us to deconvolve the fields:

$$\hat{\delta}_{\text{rec}}^{\text{dec}}(\mathbf{k}, z) = \mathcal{K}(k, z) \hat{\delta}_D^{\text{rec}}(\mathbf{k}, z). \quad (31)$$

We define a normalised cross-correlation between two fields by

$$G(k, z) = \frac{\langle \hat{\delta}_{\text{rec}}^{\text{dec}}(\mathbf{k}, z) \overline{\hat{\delta}^{\text{LIN}}(\mathbf{k})} \rangle}{P^{\text{LIN}}(k)} = \frac{\langle \hat{\delta}_D^{\text{rec}}(\mathbf{k}, z) \overline{\hat{\delta}^{\text{LIN}}(\mathbf{k})} \rangle}{\sqrt{P_D^{\text{rec}}(k, z)} \sqrt{P^{\text{LIN}}(k)}}. \quad (32)$$

We compute  $G(k, z)$  for the simulation at redshift  $z = 0.5$  represented by the red curve in Fig. 8. Any reconstruction should yield larger values than this curve. We find that the lognormal reconstruction in green gains information, however introduces a small systematic deviations on large scales (deviations from 1 at scales  $k \lesssim 0.05$ ). A similar result is obtained by linearising the field at  $z = 0.5$  with LPT (magenta curve) as described in §3 (1st equation). The advantage of this linearisation is that it does not introduce systematic effects on large scales. We then trace this field backw in time with ELPT to different redshifts:  $z = 1$  (cyan),  $z = 2$  (blue) and  $z = 10$  (black). We can see that there is an important

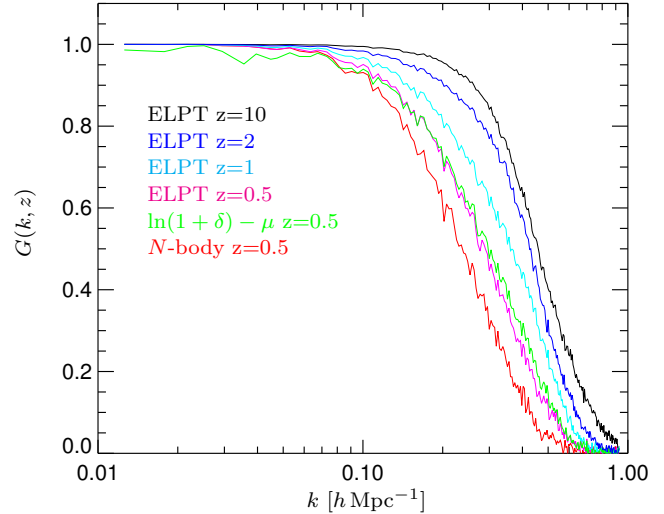


**Figure 8.** Normalised cross-correlation between the simulation at redshift 127 and: the simulation at  $z = 0.5$  (red curve), the lognormal transformation (green curve) and the ELPT reconstructions at  $z = 0.5, 1, 2, 10$  (magenta, cyan, blue and black, respectively).

gain of information between  $z = 0.5$  and  $z = 2$ . However, this gain becomes rather moderate when going to even larger redshifts. We have checked that the Baryon Acoustic Oscillations are significantly recovered as expected from the cross-correlation results. We will however, present a more detailed study on this based on a large volume  $N$ -body simulation.

## 5 CONCLUSIONS

In this work we have investigated the linearisation of cosmic density fields with nonlocal Lagrangian perturbation theory and local rank ordering mapping by a lognormal transform.

Let us summarise the implications of our findings in a series of points:

- (i) Linearisation of cosmic density fields yields estimates of the initial conditions of the Universe in Eulerian coordinates, i. e. in the coordinates in which structures are located at present.
- (ii) The relation between the density field and its linear component is nonlinear and nonlocal. Local rank ordered mapping relations like the lognormal transformation although working overall fine can introduce systematics on large scales not present in the original fields.
- (iii) The linear component in Eulerian coordinates can be used to estimate the peculiar velocity field or the displacement field using Lagrangian perturbation theory. We further demonstrate this in a companion paper (Kitaura et al. 2011). Note, that the use of the lognormal approximation to obtain an estimate of the linear displacement field has been demonstrated in an independent recent work (Falck et al. 2011).
- (iv) The linear component is more correlated with the initial conditions than the full gravitationally evolved density field and has a potential use to better constrain cosmological parameters. This has already been shown by Neyrinck et al.

(2011) for the lognormal case. The LPT linearisation should be even more accurate as it takes the nonlocal tidal field component into account. This point remains to be further studied and quantified.

(v) The linear component can be accurately traced back in time on large-scales  $\gtrsim 5 h^{-1}\text{Mpc}$  from Eulerian to Lagrangian coordinates yielding significantly more correlated fields with the initial conditions than the Eulerian representation. This implies that Eulerian grid-based methods (as opposed to particle based methods, see Peebles 1989; Nusser & Branchini 2000; Branchini et al. 2002; Eisenstein et al. 2007; Lavaux et al. 2008) could be used to recover Baryon Acoustic Oscillations or other physical signals.

(vi) We have demonstrated that one can compute the nonlinear component from the linear component with LPT. It was shown in Kitaura et al. (2010) (see appendix A) how to do that in the lognormal approximation even for the case in which the mean field is not known. This can be useful for various reasons. It is easier to obtain estimates of the linear component than of the full nonlinear density field from observational data. The reason being that modeling the power-spectrum (or two-point correlation function) in the reconstruction method is easier than including higher-order correlation functions (see Kitaura 2010). It was demonstrated in Kitaura et al. (2010) how to transform the density field into its linear component to apply a Gaussian prior and determine the power-spectrum iteratively. One could use the same concept with more complex relations between the density field and its linear component like the one provided by LPT discussed in this work.

In summary, we have shown how to apply higher order Lagrangian perturbation theory to gravitationally evolved fields and discussed the manifold of applications which can be further developed based on this approach.

## ACKNOWLEDGMENTS

We thank S. D. M. White for encouraging conversations. Warm thanks to Volker Müller for his comments on the manuscript. We are indebted to the German Astrophysical Virtual Observatory (GAVO) and the MPA facilities for providing us the Millennium Run simulation data. The work of REA was supported by Advanced Grant 246797 "GALFORMOD" from the European Research Council.

## REFERENCES

- Angulo R. E., White S. D. M., 2010, *MNRAS*, 405, 143  
 Bernardeau F., Colombi S., Gaztañaga E., Scoccimarro R., 2002, *Phys.Rep.*, 367, 1  
 Blake C., Collister A., Bridle S., Lahav O., 2007, *MNRAS*, 374, 1527  
 Blake C., Davis T., Poole G. B., Parkinson D., Brough S., Colless M., Contreras C., Couch W., et al., 2011, *MNRAS*, 415, 2892  
 Bouchet F. R., Colombi S., Hivon E., Juszkiewicz R., 1995, *Astr.Astrophys.*, 296, 575  
 Branchini E., Eldar A., Nusser A., 2002, *MNRAS*, 335, 53  
 Buchert T., Melott A. L., Weiss A. G., 1994, *Astr.Astrophys.*, 288, 349  
 Cole S., Percival W. J., Peacock J. A., Norberg P., Baugh C. M., Frenk C. S., Baldry I., Bland-Hawthorn J., et al., 2005, *MNRAS*, 362, 505  
 Coles P., Jones B., 1991, *MNRAS*, 248, 1  
 Eisenstein D. J., Seo H.-J., Sirko E., Spergel D. N., 2007, *ApJ*, 664, 675  
 Eisenstein D. J., Zehavi I., Hogg D. W., Scoccimarro R., Blanton M. R., Nichol R. C., Scranton R., Seo H.-J. a., et al., 2005, *ApJ*, 633, 560  
 Falck B. L., Neyrinck M. C., Aragon-Calvo M. A., Lavaux G., Szalay A. S., 2011, *ArXiv e-prints*  
 Gramann M., 1993, *ApJ*, 405, 449  
 Hütsi G., 2006, *Astr.Astrophys.*, 459, 375  
 Joachimi B., Taylor A. N., Kiessling A., 2011, *ArXiv e-prints*  
 Kitaura F., Jasche J., Metcalf R. B., 2010, *MNRAS*, 403, 589  
 Kitaura F. S., 2010, *ArXiv e-prints*  
 Kitaura F.-S., Angulo R., Hoffman Y., Gottlober S., , 2011, in preparation  
 Kitaura F.-S., Gallerani S., Ferrara A., 2010, *ArXiv e-prints*  
 Lavaux G., Mohayaee R., Colombi S., Tully R. B., Bernardeau F., Silk J., 2008, *MNRAS*, 383, 1292  
 Matarrese S., Lucchin F., Moscardini L., Saez D., 1992, *MNRAS*, 259, 437  
 Mehta K. T., Seo H.-J., Eckel J., Eisenstein D. J., Metchnik M., Pinto P., Xu X., 2011, *ApJ*, 734, 94  
 Monaco P., Efstathiou G., 1999, *MNRAS*, 308, 763  
 Neyrinck M. C., Szapudi I., Szalay A. S., 2009, *ApJ*, 698, L90  
 Neyrinck M. C., Szapudi I., Szalay A. S., 2011, *ApJ*, 731, 116  
 Noh Y., White M., Padmanabhan N., 2009, *Phys. Rev. D*, 80, 123501  
 Nusser A., Branchini E., 2000, *MNRAS*, 313, 587  
 Nusser A., Dekel A., 1992, *ApJ*, 391, 443  
 Peebles P. J. E., 1989, *ApJ*, 344, L53  
 Percival W. J., Reid B. A., Eisenstein D. J., Bahcall N. A., Budavari T., Frieman J. A., Fukugita M., Gunn J. E., et al., 2010, *MNRAS*, 401, 2148  
 Rimes C. D., Hamilton A. J. S., 2005, *MNRAS*, 360, L82  
 Rimes C. D., Hamilton A. J. S., 2006, *MNRAS*, 371, 1205  
 Scoccimarro R., 1998, *MNRAS*, 299, 1097  
 Springel V., White S. D. M., Jenkins A., Frenk C. S., Yoshida N., Gao L., Navarro J., Thacker R., et al., 2005, *Nature*, 435, 629  
 Weinberg D. H., 1992, *MNRAS*, 254, 315  
 Yu Y., Zhang P., Lin W., Cui W., Fry J. N., 2011, *ArXiv e-prints*  
 Zhang T.-J., Yu H.-R., Harnois-Déraps J., MacDonald I., Pen U.-L., 2011, *ApJ*, 728, 35